Density muon radiography of La Soufrière of Guadeloupe volcano: comparison with geological, electrical resistivity and gravity data

N. Lesparre, Dominique Gibert, Jacques Marteau, Jean-Christophe Komorowski, Florence Nicollin, Olivier Coutant

Geophysical Journal International

Geophys. J. Int. (2012) **190,** 1008–1019 doi: 10.1111/j.1365-246X.2012.05546.x

Density muon radiography of La Soufrière of Guadeloupe volcano: comparison with geological, electrical resistivity and gravity data

Nolwenn Lesparre,[1*] Dominique Gibert,[1] Jacques Marteau,[2] Jean-Christophe Komorowski,[1] Florence Nicollin[3] and Olivier Coutant[4]

[1]*Institut de Physique du Globe de Paris (UMR CNRS* 7154*), Sorbonne Paris Cité, Paris, France. E-mail: gibert@univ-rennes1.fr*
[2]*Institut de Physique Nucléaire de Lyon (UMR CNRS* 5822*), Lyon, France*
[3]*Géosciences Rennes (UMR CNRS* 6118*), Rennes, France*
[4]*Institut des Sciences de la Terre (UMR CNRS* 5275*, IRD UR* 219*), Grenoble, France*

Accepted 2012 May 15. Received 2012 May 3; in original form 2012 January 7

GJI Mineral physics, rheology, heat flow and volcanology

SUMMARY

Density muon radiography is a new method to determine the average density of geological bodies by measuring the attenuation produced by rocks on the flux of cosmic muons. We present such density radiographies obtained for the Soufrière of Guadeloupe lava dome, both in the north–south and east–west planes. These radiographies reveal the highly heterogeneous density structure of the volcano, with low-density regions corresponding to recognized hydrothermally altered areas. The main structures observed in the density radiographies correlate with anomalies in electrical resistivity cross-sections and a density model obtained from gravity data.

Key words: Tomography; Gravity anomalies and Earth structure; Electrical properties; Hydrothermal systems; Volcano monitoring; Volcanic hazards and risks.

1 INTRODUCTION

Quantifying eruption hazards fundamentally consists in placing the present state of a volcano in its phase space to answer the question: *how is the present state of the volcano far from a destabilization state*? In practice, the phase space is constructed with geological data which provide information concerning the various destabilization scenarios which occurred in the past and may happen again. Geological data also give insights on timescales and recurrence periods for the different classes of events—flank destabilization, phreatic eruption, magmato-phreatic explosion, . . . —to get estimates of their occurrence probabilities. This general framework may eventually be refined by using geophysical and geochemical data to obtain an as precise as possible characterization of the present state of the volcano and determine its instantaneous evolution trajectory in the phase space through monitoring. The knowledge of the volcano interior constitutes a major issue to reach these goals by providing images of the structures and of the plumbing system, in relation with fluid transport (magma, gas or water) or physical and chemical evolution of the volcanic materials (e.g. hydrothermal alteration).

Geophysical imaging of volcanoes remains a challenging issue because their highly heterogeneous 3-D structure necessitates a high-density data sampling to be performed in difficult fields conditions, and also poses specific difficulties like, for instance, strong wave scattering and attenuation, and high resistivity contrasts making data inversion highly non-linear. Some physical properties may be imaged with different geophysical methods having their own advantages and disadvantages. For instance, electrical properties may be imaged through DC electrical resistivity (e.g. Pessel & Gibert 2003), low-frequency electromagnetic techniques (e.g. Zhdanov 2009), geological radar (e.g. Leparoux *et al.* 2001), and spontaneous potential (Maineult *et al.* 2006; Kirsch & Yaramanci 2009). Identically, mechanical properties like elastic parameters may be imaged with seismic reflection or refraction methods, transmission tomography, seismic noise or active sources, etc. Within this respect, rock density is, up to now, mainly determined by means of gravity measurements whose inversion suffers from strong nonuniqueness and low-resolution performances (e.g. Li & Oldenburg 1998; Calcagno *et al.* 2008; Guillen *et al.* 2008).

The recently developed muon tomography method interestingly reinforces gravity methods by providing a new means to determine the density of large volumes of rock by using the attenuation of the flux of cosmic muons crossing the geological body of interest (e.g. Nagamine 2003). The small cross-section of muons (Barrett *et al.* 1952) and their energy range (Gaisser & Stanev 2008) allow to probe geological objects at kilometre scales in a reasonable amount of time (Lesparre *et al.* 2010). Muon tomography presently benefits from a growing interest and, since the pioneering studies by Nagamine 1995, Nagamine *et al.* (1995), several studies appeared which demonstrate the interest of the method to image spatial and

*Now at: Systems and Computer Engineering, Carleton University, Ottawa, Canada.

temporal variations of the density inside volcanoes (Tanaka *et al.* 2005, 2007a,b, 2008, 2009a,b, and references therein). However, comparisons of muon tomography imaging with other geophysical data remain scarce, and the work by Caffau *et al.* (1997) who compared muon radiography with gravity measurements remains an exception. It is one objective of the present paper to provide a qualitative comparison with electrical resistivity and gravity data acquired on La Soufrière of Guadeloupe volcano which is one of the most hazardous in the Lesser Antilles volcanic arc for which density muon tomography is of great interest (Gibert *et al.* 2010). A quantitative joined inversion of muon radiographies with resistivity and gravity data necessitates further field experiments and will be the subject of a forthcoming study.

The paper is organized as follows: Section 2 recalls the main phases of the eruptive history of La Soufrière and enumerates the hazards represented by this volcano. Section 3 describes the telescope and gives details on the field experiments. Section 4 presents the data and explains the main steps of the data processing leading to the production of average-density radiographies of the volcano. Section 5 discuss the muon density radiographies against geological informations and geo-electrical and gravity data available for La Soufrière.

2 LA SOUFRIÈRE ERUPTIVE HISTORY AND HAZARDS

La Soufrière of Guadeloupe is a stratovolcano that belongs to the Lesser Antilles volcanic arc which counts a dozen of either potentially or presently active volcanoes located in populated areas. Historical records of lesser Antilles volcanoes dating back to 1632 AD are very short compared to their eruptive frequency of a few hundreds of years. In addition, limited volcano monitoring networks which began only in the 1950's were significantly improved in the last few decades as a result of the 1976–77 eruptive crisis of la Soufrière of Guadeloupe, the 1979 eruption of Soufrière of St. Vincent and particularly in the current ongoing 15 year-long eruption of Soufrière Hills of Montserrat. Indeed this is a major difficulty as most of these active volcanoes have not undergone a magmatic eruption in the historical period and even less so since adequate multiparameter monitoring network were implemented. The last magmatic eruption at la Soufrière of Guadeloupe is dated 1530 AD (Boudon *et al.* 2008; Komorowski *et al.* 2008) and corresponds to the formation of the present lava dome whose area is represented in light grey on Fig. 1.

The last 12 000 yr of activity of La Soufrière are characterized by a succession of lava dome eruptions with explosive phases intercalated with prolonged periods of ash-producing phreatic explosive activity and an exceptional recurrence of small-volume edifice collapses that emplaced at least 12 debris-avalanches on the SE and principally the SW flanks of the volcano to a distance of 10 km (Komorowski *et al.* 2002, 2005; Boudon *et al.* 2007). In historical times, six phreatic eruptions have been recorded at la Soufrière of Guadeloupe in 1690, 1797–1798, 1809–1812, 1836–1837, 1956, and 1976–1977, involving different sectors of the lava dome particularly in the northern and eastern sides (Fig. 1). The last 1976–1977 eruption has been interpreted as a stillborn or failed magmatic eruption (Feuillard *et al.* 1983; Komorowski *et al.* 2005; Villemant *et al.* 2005; Boichu *et al.* 2008, 2011) linked to the intrusion of a small volume of viscous andesitic magma that stopped within a few kilometres of the surface triggering pressurization of the hydrothermal system, phreatic explosions and continuing episodic chlorine degassing into the hydrothermal system (Villemant *et al.* 2005).

In the last decade the Guadeloupe Volcanological and Seismological Observatory (OVSG-IPGP) has recorded a systematic progressive increase in shallow low-energy seismicity, a slow rise of temperatures of some acid-sulfate thermal springs (Villemant *et al.* 2005) closest to the dome (Figs 1 and 2), and, most notably, a significant increase in the flux of summit fumarolic activity associated with HCl-rich and H_2S acid gas emanations (Komorowski *et al.* 2001; OVSG 1999–2011; Komorowski *et al.* 2005). No other anomalous geophysical signals have been recorded such as significant ground deformation, deep-seated volcanic seismicity or significant SO_2 gas emissions. This new period of unrest motivated the increase of the alert level from 1 (green; no alert) to level 2 (yellow; vigilance). Given the societal impacts of any renewed activity, an extensive multiparameter monitoring network is operated by the Observatoire Volcanologique et Sismologique de Guadeloupe (OVSG) of the Institut de Physique du Globe de Paris (IPGP). It is dedicated to understand the current behaviour of the hydrothermal-magmatic systems and to detect changes in their base level activity that could constitute possible precursory signs of an impending phreatic eruption or the ascent of a magmatic intrusion that could lead to a new magmatic eruption. Given the Holocene record of partial flank instability, any of these unrest scenarios (phreatic or magmatic) can be associated with renewed partial flank collapse and sudden explosive decompression of pressurized volatiles of either hydrothermal or magmatic origin. The OVSG (IPGP) also provides a research and analytical platform to test new methods which could ultimately be integrated to the routine set of tools and techniques used for volcano surveillance at La Soufrière but also at other analogue volcanoes in the world.

Knowledge of the density distribution inside La Soufrière is particularly important to constrain its mechanical behaviour in case of pressurization of hydrothermal and/or magmatic volatiles and flank destabilization. The structure of la Soufrière volcano has been significantly affected by both phreatic explosions which opened fractures and by hydrothermal acid fluids which have transformed the original volcanic rocks (andesite, ashes) into mechanically weak hydrothermalized material. Moreover these processes have led to the formation of low strength layers in the dome where shear friction is reduced and pore fluid pressure can be increased by the preferential circulation of hydrothermal fluids (Fig. 2). Hence, it is important to obtain an image of the internal structure, geometry and mechanical nature of rocks that form the La Soufrière dome to determine the volumes of material involved in case of flank destabilization. This objective can be achieved by undertaking a global density tomography of the dome. Implementing a time-series of continuous density tomography is necessary to follow density variations that are associated with fluid movements in the volcano and possibly related to liquid/vapour transformation in the shallow hydrothermal system.

3 DESCRIPTION OF FIELD EXPERIMENTS

3.1 Main characteristics of the telescope

The telescope deployed for the experiments discussed in this study is equipped with three matrices composed of $N_x = 16$ horizontal and $N_y = 16$ vertical scintillator strips whose intersections define 256 pixels with an area of $5 \times 5\,\mathrm{cm}^2$ (left of Fig. 3). A detailed

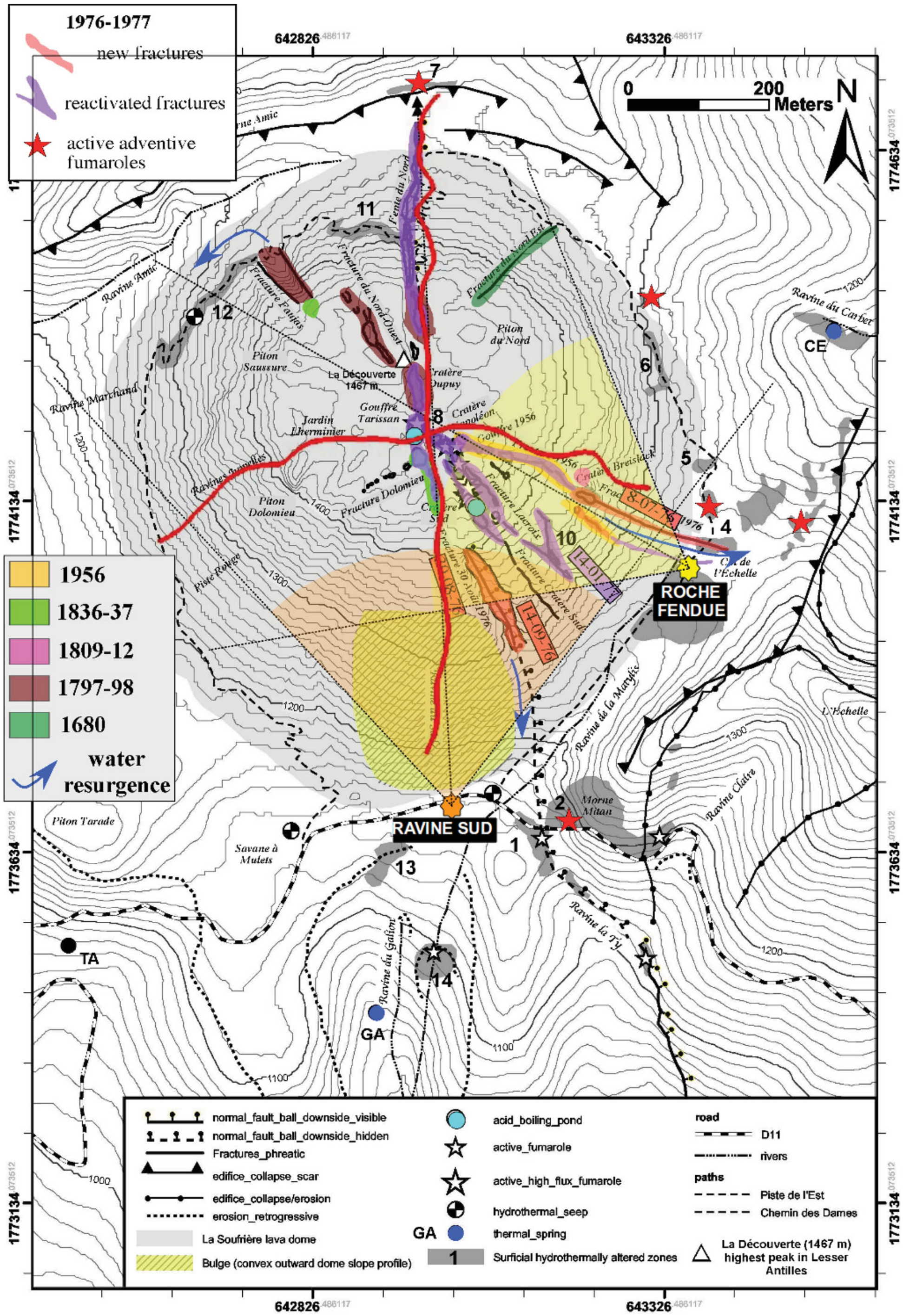

Figure 1. Map of the location of the main structures, historical eruptive vents, and sites of currently observed fumarolic activity on La Soufrière lava dome (Komorowski 2008, modified after Nicollin *et al.* 2006). The two locations occupied by the telescope, Ravine Sud and Roche Fendue, are shown. The angular range spanned by the telescope at each location is represented as faint coloured sectors with they apex pointing on the location of the telescope. The resistivity profiles corresponding to the pseudo-sections of apparent resistivity of Fig. 8 are represented as solid red curves. The area corresponding to the lava dome is represented in light grey.

description of our field telescopes is given by Marteau *et al.* (2011) and we here recall only their main characteristics.

When a charged particle—muon, pion, electron—hits a scintillator strip, ionization occurs and a light pulse is emitted when the ionized atoms return to their low-energy state. In the case of a muon, an energy input of about 2 MeV is left in a scintillator bar of 1 cm in thickness and about 10^5 photons are emitted. The resulting light pulse is captured by optic fibres and detected by a photomultiplier.

The muon trajectory is determined by the pair of pixels $(a_{i,j}, b_{k,l})$ fired by the particle, where $a_{i,j}$ is a pixel belonging to the front matrix A and $b_{k,l}$ belongs to the rear matrix B. Here, indexes i, k vary from 1 to N_x and j, l vary from 1 to N_y. The combination of

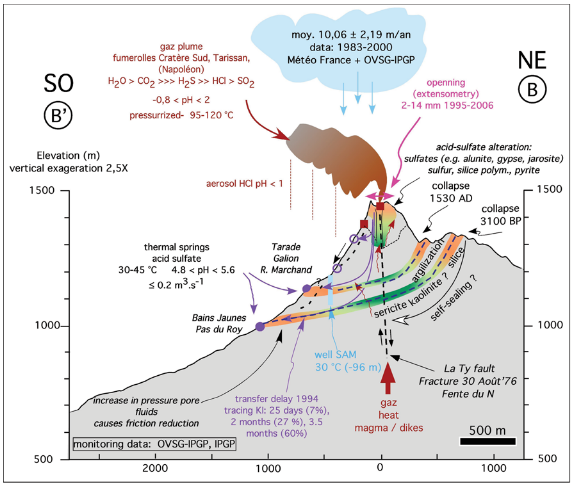

Figure 2. Cross-section showing the conceptual structure of the shallow hydrothermal system of La Soufrière. The dashed lines and the purple arrows represent flow paths of hydrothermal fluids. The colour gradient represents the transition of hydrothermal alteration from oxidizing (orange) to reducing conditions (green). (After Komorowski 2008; see also Salaün *et al.* 2011.)

all possible pairs of pixels ($a_{i,j}$, $b_{k,l}$) defines a set of $(2N_x - 1) \times (2N_y - 1) = 961$ discrete directions of sight $\mathbf{r}_{m,n}$, where the indexes $m = i - k$ and $n = j - l$ only depend on the relative shift between the $a_{i,j}$ and $b_{k,l}$ pixels. The angular range spanned by the 961 directions may be controlled by adjusting the distance between the front and rear matrices. For the present experiments, this distance was kept constant at $D = 95$ cm corresponding to an angular aperture of 77° and an average resolution of 2.5° both in the horizontal and vertical planes. The retained angular aperture allows to scan most of the lava dome from a single viewpoint located near the volcano (Fig. 4). The angular resolution corresponds to a space resolution $\delta l = 22$ m at a distance $L = 500$ m from the telescope.

Fortuitous events caused by two particles simultaneously hitting the matrices A and B may cause a huge noise masking the faint variations of flux caused by the density heterogeneities inside the volcano. The occurrence probability of fortuitous events may be considerably reduced by using a third detection matrix C located in between matrices A and B (left-hand side of Fig. 3), and by keeping only those events whose three fired pixels (a, b, c) are aligned.

Other undesirable events may be caused by atmospheric electrons with sufficient energy to cross the three matrices (Nagamine 2003). These events may be suppressed by using an iron shielding (black plate on left-hand side picture of Fig. 3) placed against the median matrix and whose thickness is sufficient to either stop the electron or produce an electron shower causing multiple events on either matrix A or B. In this study, the thickness of the shielding equals 24 mm.

The telescope is an autonomous instrument with a total power consumption of 40 W provided by solar panels with a peak power of 720 W (middle of Fig. 3). The discrepancy between telescope power and solar unit power is due to the cloudy weather encountered on La Soufrière which necessitates a security factor of ≈20 to ensure a continuous operation of the telescope. However, despite this security margin very cloudy periods occur during the hurricane season and failure of the electrical power units may occur for several days. To manage these events, the telescope is equipped with remotely controllable relays which may be activated to turn off devices of the telescope and reduce the power consumption until the electrical accumulators remain filled.

The telescope is equipped with a number of sensors—electrical current, voltages, temperature, relative humidity, inclinometers—which provide information concerning the nominal operation of the instrument. These sensors are connected to an independent data logger plugged on the wireless link to automatically upload data on the Volcano Observatory database.

The total weight of the equipment is ≈800 kg, including solar panels, accumulators and iron shielding. The heaviest elements are the detector matrices with a weight of 45 kg. All elements are rugged enough to support helicopter hauling (right-hand side of Fig. 3) and even transportation through rope access techniques on very rough topography. A thick tarpaulin ensures a protection against the heavy tropical rains (middle of Fig. 3), and guys are used to secure the telescope against gusts.

3.2 Measurement sites

The data discussed in this paper have been acquired by installing the telescope at two locations hereafter referred to as the Ravine Sud and the Roche Fendue sites (Fig. 1). These sites are respectively located on the southern and eastern sides of the lava dome

Figure 3. Left-hand side: view of the telescope equipped with three scintillator matrices. The iron shielding is the black plate placed against the central matrix. The aluminium box contains electronic devices: data logger, DC–DC converters, reference clock, ethernet switch, main computer. Middle: general view of the installation at the Roche Fendue site. Three solar units each with peak power of 270 W are necessary because of the quasi permanent cloudy weather. The telescope is equipped with its green tarpaulin and ready for measurements. Right-hand side: moving of the telescope from the Ravine Sud site toward the Roche Fendue place.

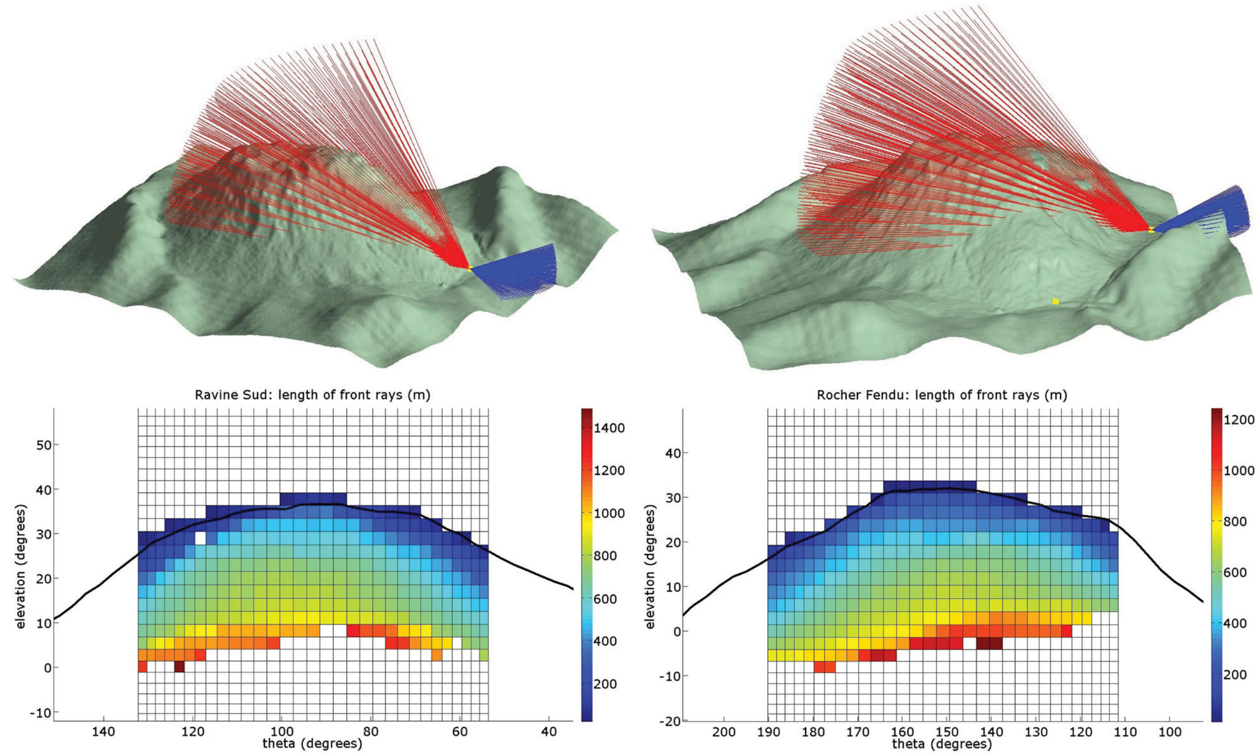

Figure 4. Top panel: ray distribution for the Ravine Sud site (left-hand side) and the Roche Fendue site (right-hand side). Backward rays are shown in blue. Bottom panel: length L (m) of the rays crossing the lava dome from the Ravine Sud site (left-hand side) and the Roche Fendue site (right-hand side).

Table 1. Telescope parameters.

	Ravine Sud	Roche Fendue
Altitude a.s.l.	1163 m	1268 m
X_{UTM} WGS84	(20)643033 m	(20)643347 m
Y_{UTM} WGS84	1773714 m	1774036 m
Distance to observatory	8.29 km	7.85 km
Zenith angle	67.0°	75.2°
Azimuth	−3.0°	299.1°
Number of matrices	3	3
Matrix distance	47.5 cm	47.5 cm
Angular resolution	2.5°	2.5°
Resolution at dome centre	20 m	20 m
Iron shield thickness	24 mm	24 mm
Acquisition time	82 d	83 d

and are in direct sight of the Volcano Observatory, allowing an easy implementation of radio link for both data transmission and remote control of the telescope. The two sites also present the great advantage that no perturbing mountain is present behind the lava dome to produce perturbing shadows on the radiographies. Table 1 recalls the principal parameters about both sites.

The telescope was first installed at the Ravine Sud site located on the edge of the road along the southern side of the lava dome at an altitude of 1163 m (Fig. 1). The rays crossing the dome from this site have a maximum length $L \sim 1000$ m (bottom left-hand side of Fig. 4) and span a zenith angle range $55° \le \theta \le 80°$. The landscape south of the dome—that is, in the back of the telescope when oriented northward toward the volcano—is made of the large valley of the Galion river in the forefront and of the Caribean Mounts in the background at a distance of ∼10 km. This configuration is such that the whole sky is clear from obstacles in the back of the telescope. This allows measurements of the backward flux of muons for a limited range of zenith angles (top left of Fig. 4).

The Roche Fendue site (Fig. 1) is less accessible and helicopter hauling was used to move the equipment at this place (Fig. 3 right-hand side). As can be seen on the bottom right-hand side part of Fig. 4, the ray lengths are slightly smaller, $L \sim 700$ m, than for the Ravine Sud site. The crossing rays span a zenith angle range $60° \le \theta \le 80°$. The western side of the volcano, opposite to the telescope, is clear from mountains which could produce perturbing shadows on the radiographies. Contrarily to the situation encountered at the Ravine Sud place, the backward directions of sight of the telescope fall into the Échelle mountain which screens the intense flux from the open sky.

3.3 Measurement characteristics

The number of muons ν, detected by the telescope is given by (Lesparre *et al.* 2010),

$$\nu(\mathbf{r}_{m,n}, \Delta T) = I(\mathbf{r}_{m,n}) \times \Delta T \times \mathcal{T}(\mathbf{r}_{m,n}), \tag{1}$$

where I is the muon flux (cm^{-2} sr^{-1} s^{-1}) given by eq. (2), ΔT is the measurement duration (s), and $\mathcal{T}$ (cm^2 sr) is the acceptance function of the telescope.

The acceptance quantifies the telescope capability to capture a flux coming from a given solid angle centred in a given direction. The acceptance depends on the geometrical characteristics of the telescope and is shown in Fig. 5 for all 961 discrete directions $\mathbf{r}_{m,n}$, $N_x = N_y = 16$, $D = 95$ cm, and pixel size $d = 5^2$ cm^2. As expected, the acceptance is maximum (≈18.3 cm^{2}sr) for the direction $\mathbf{r}_{0,0}$ perpendicular to the matrices since all pixels contribute to the detection surface.

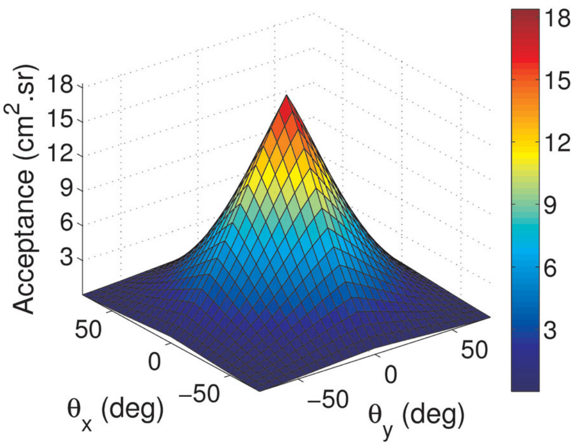

Figure 5. Acceptance $\mathcal{T}$ of the telescope as a function of the direction of sight **r** and for a matrix distance of 95 cm. The maximum at the centre of the plot corresponds to the direction of sight $\mathbf{r}_{0,0}$ perpendicular to the detection matrices.

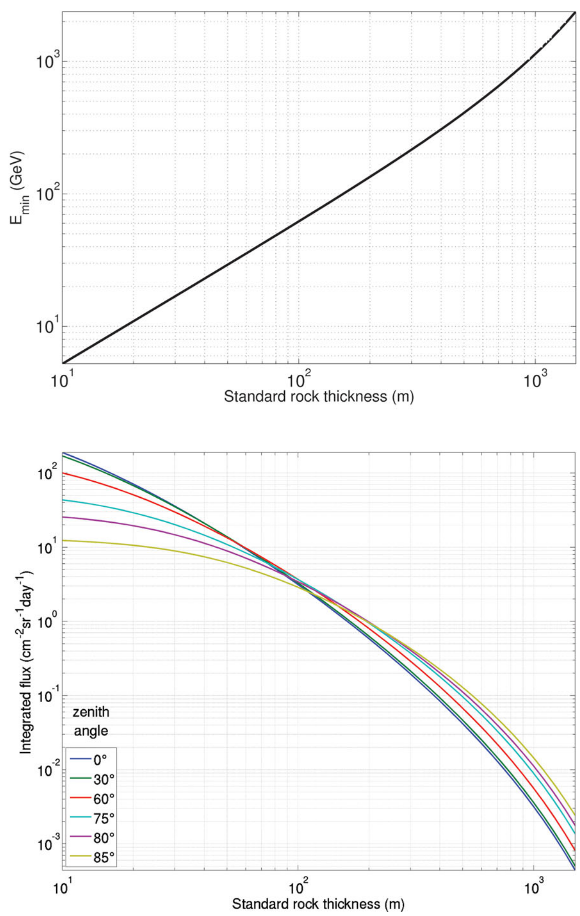

Figure 6. Top panel: minimum energy $E_{\rm min}$ as a function of crossed thickness of standard rock (i.e. with $\rho = 2.65$ g.cm^{-3}). Bottom panel: integrated flux, $I[\varrho, \theta]$ (eq. 2), as a function of crossed thickness of standard rock and for several zenith angles θ.

The integrated flux of muons, I, emerging from the lava dome after crossing its rock mass is controlled by the incident differential flux, Φ_0 (cm^{-2} sr^{-1} s^{-1} GeV^{-1}), and by the minimum energy, $E_{\rm min}$ (GeV), necessary for a muon to cross a given amount of matter ϱ (hg cm^{-2}) (Fig. 6):

$$I[\varrho, \theta] = \int_{E_{\rm min}(\varrho)}^{\infty} \Phi_0(E, \theta)\mathrm{d}E \quad [\mathrm{cm}^{-2}\mathrm{sr}^{-1}\mathrm{s}^{-1}]. \tag{2}$$

In eq. (2), θ is the zenith angle which is the main parameter controlling the intensity of Φ_0 (Gaisser & Stanev 2008). A discussion concerning the models available for Φ_0 may be found in Lesparre *et al.* (2010) and, in this study, we use the model given by Tang *et al.* (2006).

The amount of matter, hereafter called the opacity, to be crossed by the muons is defined as

$$\varrho(L) = \int_L \rho(\xi)\mathrm{d}\xi = \overline{\rho} \times L, \tag{3}$$

where ξ is the coordinate measured along the ray trajectory of length L crossing the volcano (Fig. 4), ρ is the density and $\overline{\rho}$ is the density averaged along the trajectory. In practice, ϱ is often expressed in hg cm^{-2}, a physical unit which corresponds to 1 m water equivalent (m w.e.). Another useful unit for ϱ is 2.65 hg cm^{-2} which corresponds to equivalent metres of standard rock (m s.r.e.) as defined by the Particle Data Group (e.g. Kudryavtsev 2009) and used in Fig. 6.

Lesparre *et al.* (2010) established a condition to be satisfied to distinguish a variation $\delta\varrho$ through a geological body of opacity ϱ_0 for a given telescope acceptance, $\mathcal{T}$, and measurement duration ΔT:

$$\Delta T \times \mathcal{T} \times \frac{\Delta I^2(\varrho_0, \delta\varrho)}{I(\varrho_0)} > c. \tag{4}$$

Here ΔI^2 is the variation of integrated flux caused by the opacity variation $\delta\varrho$ inside an object of total opacity ϱ_0. The value chosen for the right-hand term of eq. (4) fixes the confidence level of the resolution achieved on $\delta\varrho$ with $c = 1$ corresponding to one standard deviation (i.e. about 68 per cent).

Taking a typical ray length $L = 800$ m and an average density $\overline{\rho} = 2.0$ g cm^{-3} give $\varrho_0 = 600$ m s.r.e. (eq. 3) and $I \approx 0.1$ cm^{-2} sr^{-1} day^{-1} for zenith angles $\theta \approx 75^\circ$ (Fig. 6). With such an integrated flux and a typical telescope acceptance $\mathcal{T} = 10$ cm^2 sr, eq. (1) gives $\nu = 1$ muons detected every day per direction of sight. Now, decreasing the average density by 10 per cent gives $\delta\varrho = 60$ m s.r.e. and an integrated flux variation $\Delta I \approx 0.04$ cm^{-2} sr^{-1} day^{-1}. Inserting these estimates in the feasibility formula 4, the duration of measurement must be such that $\Delta T > 2$ weeks.

4 DATA PROCESSING

4.1 Reduction of background noise

Because the telescope is placed on the ground and in open sky conditions, it is exposed to the whole particle flux of cosmic ray showers which represents a huge background noise blurring the tiny flux of muons emerging from the volcano (Nagamine 2003).

A first kind of background noise—called the uncorrelated background noise—is due to the soft component of the showers whose low-energy particles—mainly electrons and positrons—constantly hit the matrices of the telescope. If, by chance, the matrices are simultaneously hit, the logical electronic boards of the telescope will trigger the occurrence of an event. The probability of such false events may be dramatically reduced both by taking an as low as possible time resolution δt of the detector triggers and by using a telescope equipped with three matrices instead of two. Indeed, the rates of fortuitous events for two and three matrices are respectively given by (Lecomte 1963),

$$N_{\{1,2\}} = 4N_1N_2\delta t, \tag{5}$$

and,

$$N_{\{1,2,3\}} = 16 N_1 N_2 N_3 \delta t^2, \quad (6)$$

where N_1, N_2 and N_3 are the respective hit rates of matrix 1, 2 and 3, and $\delta t = 10$ ns for our telescope. These equations show that the possibility of fake tracks is anti-proportional to the number of matrices.

For la Soufrière of Guadeloupe, we measure a rate $N_i \approx 50\,\mathrm{s}^{-1}$ of events on each matrix when the telescope is configured in single-multiplicity mode, that is, all events hitting a single matrix are recorded. This rate is safely supported by the acquisition system of the telescope whose electronics readout frequency is of 5 MHz with a dead time of 13 μs after each detected event, giving a nominal bandwidth of 77 kHz. With the rates measured on the field, we find $N_{\{1,2\}} \approx 10\,\mathrm{day}^{-1}$ and $N_{\{1,2,3\}} \approx 0.007\,\mathrm{year}^{-1}$ to be compared with the rate of muons $\approx 1\,\mathrm{day}^{-1}$ expected to emerge from 600 m of standard rock. These figures could be made more precise by considering the transient higher flux of particles encountered during the passage of an extensive air shower front on the telescope (e.g. Abu-Zayyad *et al.* 2001). This necessitates a full modelling of air showers and is beyond the scope of this paper. However, the rate of fortuitous false events is further decreased by imposing the condition that the pixels triggered on the three matrices are aligned, emphasizing the absolute necessity to make measurement with three-matrices telescopes (Nagamine 2003). Another improvement will be obtained by using new electronic boards with a finer time resolution of $\delta t = 1$ ns allowing to distinguish the forward and backward directions of arrival of the particles.

A second type of noise—called the correlated background noise—is caused by particles whose energy is sufficient to make them able to cross the matrices of the telescope (Nagamine 2003). For instance, the e^+/e^- spectrum is more important than the muon spectrum at kinetic energies lower than 70 MeV (Golden *et al.* 1995) and these particles of moderate energy may easily cross the telescope whose opacity is of $9.2\,\mathrm{g\,cm^{-2}}$ (i.e. a stopping energy of 16.9 MeV). Following Nagamine (2003), we equipped the telescope with a 24 mm-thick iron screen placed against the middle matrix to increase the total opacity to $32.4\,\mathrm{g\,cm^{-2}}$ sufficient to stop e^+/e^- with a kinetic energy <108.3 MeV.

4.2 Computation of density radiographies

The first computational step consists in using eq. (1) to convert the number of events, $\nu(\mathbf{r}_{m,n})$, recorded during the detection time ΔT into the integrated flux,

$$I(\mathbf{r}_{m,n}) = \frac{\nu(\mathbf{r}_{m,n}, \Delta T)}{\Delta T \times \mathcal{T}(\mathbf{r}_{m,n})}. \quad (7)$$

As discussed in details by Lesparre *et al.* (2012), an accurate determination of the acceptance function $\mathcal{T}$ is essential to properly determine the integrated flux in eq. (7). In particular, efficiency coefficients of the scintillator strips forming the detector matrices are inverted from open-sky measurements to get an experimental acceptance function accounting for the actual characteristics of the telescope. In this study, the acceptance function is the same for both sites since the matrix arrangement was kept constant. The data were acquired during $\Delta T = 82$ d at the Ravine Sud site and $\Delta T = 83$ d at the Roche Fendue site. The number of events detected during the whole period of measurement ranges from $\approx$150 to $\approx$60 000 depending on both the acceptance and the rock thickness. Using these values, the flux computed for both sites varies between $1.7 \times 10^{-6}\,\mathrm{cm^{-2}\,sr^{-1}\,s^{-1}}$ and $8.7 \times 10^{-4}\,\mathrm{cm^{-2}\,sr^{-1}\,s^{-1}}$.

The next processing stage consists in transforming the integrated flux data into opacities by using eq. (2) to determine the opacity necessary to reproduce the observed flux (Fig. 6). We use the differential spectrum elaborated by Tang *et al.* (2006) and apply the altitude correction of Hebbeker & Timmermans (2002). In the final processing step, the opacity, ϱ, is converted into average density, $\overline{\rho}$, by using the ray length L into eq. (3). The ray length is determined from a high-resolution digital elevation model with a mesh of 2 m. The resulting average density radiographies are shown in Fig. 7 as density anomalies, $\Delta\overline{\rho}$, relative to a reference absolute density, regions with a too low signal-to-noise ratio have been removed. Both radiographies display density heterogeneities with about the same amplitude of $0.8\,\mathrm{g\,cm^{-3}}$ for an uncertainty of about 5 per cent.

The reference densities $\overline{\rho}_{\mathrm{ref}} = 1.3\ \mathrm{g\,cm^{-3}}$ for the Ravine Sud and $\overline{\rho}_{\mathrm{ref}} = 1.6\ \mathrm{g\,cm^{-3}}$ for the Roche Fendue seem negatively biased when compared with the density of rock samples. This bias may be partly explained by the presence of a residual background noise causing a positive bias in the integrated flux. To illustrate this effect, let us consider a 500 m thick layer with $\overline{\rho} = 1.8\ \mathrm{g\,cm^{-3}}$ that gives an emerging integrated flux $I = 2.9 \times 10^{-6}\,\mathrm{cm^{-2}\,sr^{-1}\,s^{-1}}$ for a zenith angle of 70°. Adding a background noise of $10^{-6}\,\mathrm{cm^{-2}\,sr^{-1}\,s^{-1}}$ to this flux gives a corresponding density of $1.6\,\mathrm{g\,cm^{-3}}$. Let us emphasize that, for an acceptance $\mathcal{T} \approx 10\ \mathrm{cm^2\,sr}$, this noise corresponds to less than one event per day for each measurement direction $\mathbf{r}_{m,n}$. The larger the thickness of rock, the smaller the emerging flux and, assuming a constant noise level, the smaller the signal-to-noise ratio and the larger the negative bias in the density. However, the radiographies of Fig. 7 do not display a systematic decrease of the density as a function of rock thickness, and no bias correction was applied. Adding a fourth matrix to the telescope would provide a means to further reduce the background noise.

The low value of $\overline{\rho}_{\mathrm{ref}}$ obtained for the Ravine Sud is possibly due to a larger noise level at this location, and we expect that this noise is due to the topography configuration of the site. In particular, the rear of the telescope is exposed to the wide (6 km) and deep (900 m) valley of the Galion River forming a large volume of air going down to −9° below the horizontal plane when seen from the telescope. This valley gives enough space for cosmic shower to produce a background flux entering the telescope by its rear face. Such a noise may not presently be removed from the data set because the clock resolution of the electronic boards is not sufficient to determine whether a particle crossed the telescope from the rear or from the front. This additional noise must be of the order of 1.4 particle per day to produce a further decrease of the density from $1.6\,\mathrm{g\,cm^{-3}}$ to $1.3\,\mathrm{g\,cm^{-3}}$. Considering this possibility, the low-density region visible at the bottom of the Ravine sud radiography may not be reliable and deserves further study.

5 COMPARISON WITH GEOLOGY, GEO-ELECTRICAL AND GRAVITY DATA

5.1 Geology

The density radiographies of Fig. 7 reveal that the lava dome is highly heterogeneous with domains of low average density $\overline{\rho} \approx 1.1\ \mathrm{g\,cm^{-3}}$ and denser regions with $\overline{\rho} \approx 1.9\ \mathrm{g\,cm^{-3}}$. Such contrasted densities are slightly lower than the densities of the various types of rocks encountered on andesitic tropical volcanoes (Bernard 1999; Komorowski *et al.* 2008). As discussed in Section 4.2, a small residual background noise may cause a

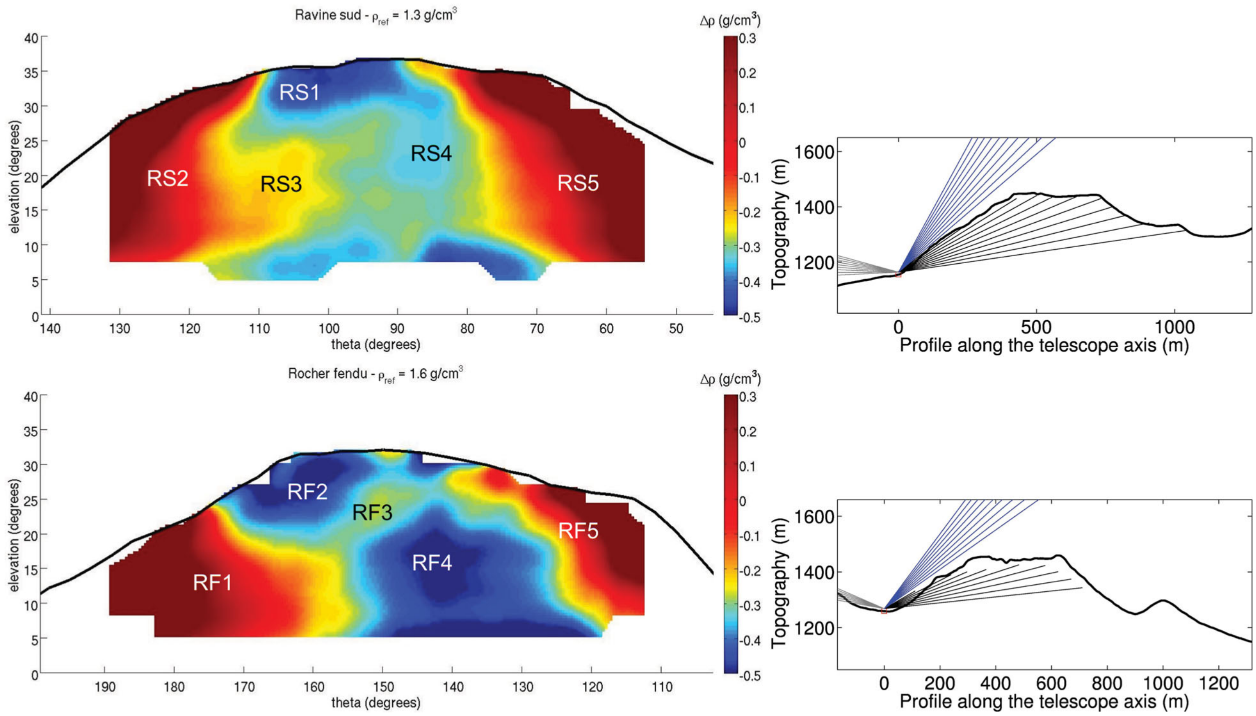

Figure 7. Left-hand side: radiographies of the average density obtained from the flux of muons measured at the Ravine Sud (top panel, west on the left-hand side) and at the Roche Fendue (bottom panel, south on the left-hand side) sites (see Fig. 4 for location). The density variations represented by the colourbar are relative to the reference density indicated in the radiography's title. Right-hand side: ray scan in the axis of the telescope. See Fig. 4 for the full ray scan pattern.

negative bias of the densities. However, it must also be considered that the densities obtained with muon radiography are averaged over huge volumes much larger than rock samples. Hence, the low average densities observed in both radiographies may at least partly be explained by the presence of voids inside the volcano. That is the case of the large low-density region RF4 located in the northern half of the dome (Fig. 7) which coincides with the large Spallanzani cave described as a series of wide cavities (L'Herminier 1815). This network of cavities is reported to extend from the Fente du Nord to the Cratère Dupuy (Fig. 1), that is, almost near the geometrical centre of the lava dome. These cavities are inaccessible since 1836 (Biot 1837) excepted for the first one whose dimensions are $55 \times 35 \times 11\,\mathrm{m}^3$ in the north–south, east–west and vertical directions, respectively (Mouret & Rodet 1985; Kuster & Silve 1997). The presence of such cavities may decrease the average density by 10–15 per cent.

Numerous other voids and caves are recognized on the summit plateau and on the flanks of the dome, the most notable being: the Dupuy and the Breislack pits, the north and the Faujas fractures, the 30 August fault, and the Tarissan and the south craters (Fig. 1). The Tarissan crater appears as a vertical chimney with a diameter of $\approx$20 m filled with a boiling acid lake whose surface is 80 m below the mouth of the crater. This crater was active during each eruptive crisis of La Soufrière and emitted most of the volume of ashes and block (e.g. about $4 \times 10^5\,\mathrm{m}^3$ during the 1976–77 crisis (Le Guern *et al.* 1980)). Kuster & Silve (1997) report that the deep penetrable part of several cavities located on the eastern flank of the lava dome (e.g. Gouffre 56 and Cratère Breislack on Fig. 1) is obstructed by fallen rock blocks that prevent further exploration but indicate that voids are likely to exist deeper in the dome. Such cavities could significantly increase the macro porosity and further reduce the average density of the dome.

The RF5 dense region forming the northern part of the Roche Fendue radiography (Fig. 7) coincides with the north and northeastern part of the dome where massive lava is observed and forms steep slopes nearby the Fracture du nord-est (overlined in dark green on Fig. 1). The RF1 dense region and its counterpart RS5 coincide with massive lava outcrops located on the southeastern flank of the dome (i.e. Fracture Lacroix overlined in purple on Fig. 1).

The RF3 region of the Roche Fendue radiography corresponds to the region located between RS1 and RS4 in the radiography of Ravine Sud (Fig. 7). This region with an intermediate density may coincide with a body of dense rock forming a barrier between the shallow RF2 hydrothermal area and the RF4 deeper one that might undergo overpressured in case of increasing energy flux coming from below. This dense barrier might also explain the appearance of active areas in the northern part of the lava dome like the Fente du nord overlined in dark purple on Fig. 1 and shown active on fig. 2(e) of Gibert *et al.* 2010) during the 1976 phreatic eruption.

5.2 Comparison with electrical resistivity data

A huge amount of electrical resistivity data was acquired on and around the lava dome during the 2001–2006 period, and a detailed description of these data is given by Nicollin *et al.* (2006). These resistivity surveys clearly reveal the heterogeneous structure of the lava dome with low conductivity regions of unaltered massive andesite and other low resistivity parts of highly hydrothermalized and unconsolidated materials. Fig. 8 shows two apparent-resistivity cross-sections in the north–south and east–west planes. The traces of these profiles are shown as red curves on Fig. 1, and the reader is referred to the paper by Nicollin *et al.* (2006) for other pseudo-sections. It can be observed that the apparent electrical resistivity

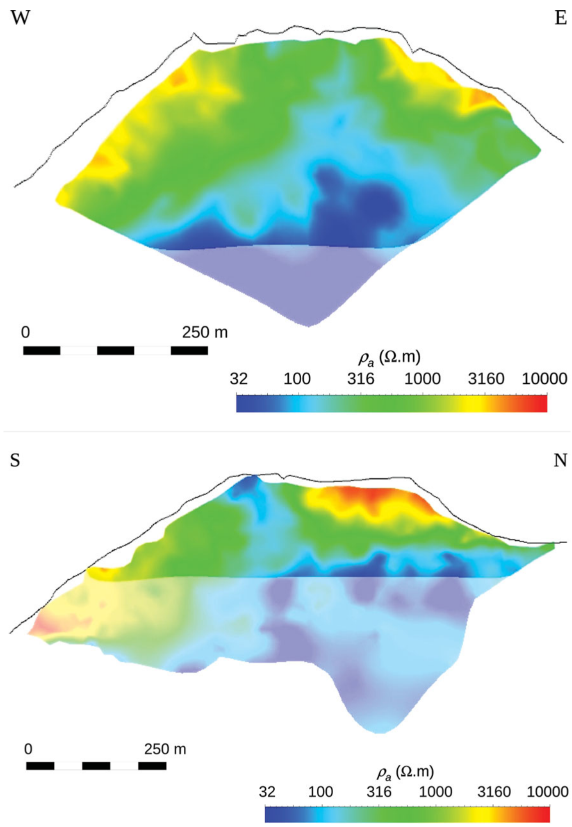

Figure 8. East–west (top panel) and north–south (bottom) cross-sections of the apparent electrical resistivity constructed with the data discussed in Nicollin *et al.* (2006). The unmasked parts of the sections approximately correspond to the domains covered by the radiographies of Fig. 7. The scale bar applies to both the horizontal and vertical axis. See Fig. 1 for the location of the corresponding profiles on the map.

varies in a wide range spanning about three orders of magnitude. Regions with very low resistivity are observed at the base of the dome and probably correspond to a layer of hydrothermalized materials. This layer is retrieved almost all around the dome basement (Nicollin *et al.* 2006). A low-resistivity 'channel' connecting the conductive lower part of the dome to the summit regions is observed on both cross-sections which have been obtained with independent data sets. This conductive channel is roughly located beneath the southeastern part of the dome summit. It most likely corresponds to the main Tarissan and Cratère Sud vents that were reactivated in all historical phreatic eruptions (Figs 1 and 2) and currently constitute the main pathways for hydrothermal fluids vertical movement and ongoing intense fumarolic degassing observed at the summit since 1992.

Although apparent-resistivity cross-sections are distorted images of the true resistivity distribution inside the volcano, both density radiographies (Fig. 7) and apparent resistivity (Fig. 8) share conspicuous features. However, the comparison must be made with caution and restricted to a qualitative interpretation of the main structures. Indeed, it must be kept in mind that the apparent resistivity sections and the average density radiographies are not representative of the same sampling volumes inside the volcano. The agreement between the main features present in both type of data indicates that the corresponding structures occupy sufficiently large parts of the volcano to intersect the sampling volumes.

The east–west resistivity cross-section and the Ravine Sud radiography display the same first-order symmetrical patterns, with more resistive zones corresponding to denser material (RS2 and RS5) on both sides of the lava dome. The vertical conductive channel going from the top of the dome down to the conductive basement has a clear low-density counterpart (RS4). This structure is shifted toward the eastern side of the volcano where a fracture network associated to the active vents is observed (Fig. 1). The very low density region RS1 located at the top of the density radiography corresponds to rays crossing the southwestern quarter of the dome and the bulge (Fig. 4) located on the southern flank of the dome and represented as a dashed yellow area above the Ravine Sud location on Fig. 1. This low density bulge is crossed by the north–south resistivity profile (Fig. 1) and corresponds to a resistive anomaly in the pseudo-section. The low density and the high electrical resistivity of the bulge together with the absence of deep extension indicate that the bulge is a superficial volume of drained material of high macro porosity.

The north–south apparent resistivity cross-section (bottom of Fig. 8) also shares many features recognized in the Roche Fendue radiography (bottom of Fig. 7). The resistive domains located on the southern and northern sides of the volcano correspond to the dense regions RF1 and RF5 in the radiography. Also, the conductive pocket located beneath the southern edge of the summit, in the South Crater area, is clearly associated with the RF2 low-density domain. The very conductive zone located deep under the northern half of the dome also corresponds to the RF4 low density region. We observe that the more resistive elongated region which separates the South Crater region from the deep conductive domain corresponds to the RF3 region of intermediate density in the radiography.

5.3 Comparison with gravity data

The gravity measurements from Gunawan (2005) have been inverted by Coutant *et al.* (2012) to derive a density model of the lava dome. The cross sections in Fig. 9 show density variations confirming the heterogeneous structure of the volcano observed in the density radiographies (Fig. 7) and in the electrical resistivity pseudo-sections (Fig. 8). By applying the method of Parasnis (1997) to its gravity data, Gunawan (2005) obtained an average density of $\approx$2.1 g cm^{-3} for the volcano above 1050 m a.s.l. This author observes that the data do not fit a single straight line in the Parasnis's diagram and concludes that the dome is probably highly heterogeneous. Core samples coming from boreholes located at the Savane à Mulets (200 m west of Ravine Sud) and Col de l'Échelle (150 m south of Roche Fendue) give densities of 2.0 g cm^{-3} for near-surface altered andesite and $\approx$2.7 g cm^{-3} for deeper massive andesite (Gunawan 2005). Altered material sampled at the summit of the lava dome have densities in the 0.9–1.3 g cm^{-3} range (F. Dufour, personal communication, 2012) . These values are very similar to those obtained by Bernard (1999) for samples of La Montagne Pelée in Martinique.

5.3.1 Ravine Sud radiography (Top panel of Fig. 7)

The northwest quarter of the gravity model of the dome appears as a high density body (D1 on Fig. 9) located beneath the most elevated part of the dome named La Découverte (Fig. 1). This dense region is crossed by the telescope rays for elevation angles $\Phi < 25°$ and $95° \leq \Theta \leq 115°$ (Top right-hand side of Fig. 7), and coincides with the medium average density region RS3 on the density radiography. At higher elevation angles, the rays no more cross the northwestern

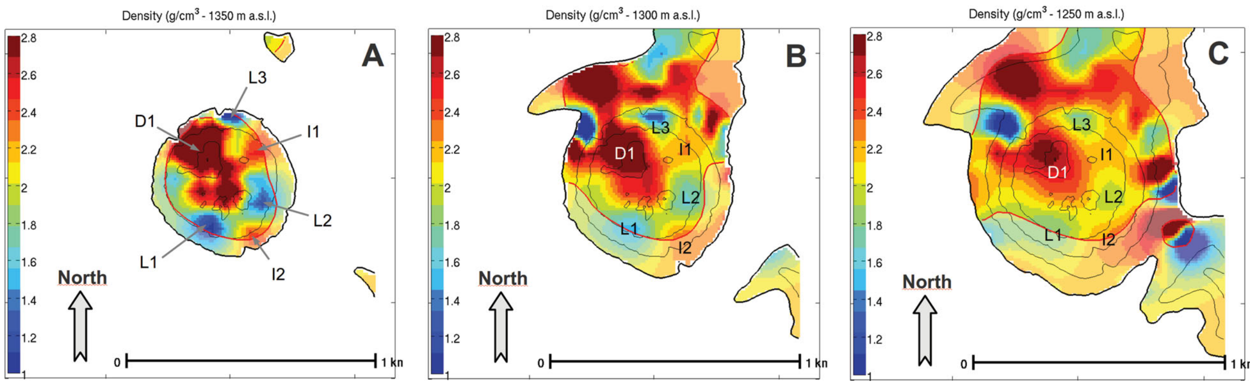

Figure 9. Horizontal cross-sections (1350, 1300 and 1250 m a.s.l.) of the density model derived by Coutant *et al.* (2012) from the gravity data by Gunawan (2005). The thick red curves separate the well-resolved regions (resolution >0.9, in bright colours) from the poorly resolved ones (in dim colours). For more details, see Coutant *et al.* (2012).

dense body seen in the gravity model but, instead, are limited to the low-density volume (L1) located in the southwestern quarter of the dome (Figs 9A and B). This corresponds to the low-density region RS1 observed in the upper part of the Ravine Sud radiography. The eastern side of the middle part of the radiography forms a vertical channel of low density (RS4) that corresponds to the low density area (L2) in the gravity model. The dense border RS2 observed on the radiography corresponds to the left part of the ray bundle (Fig. 1) that pass through the Dolomieu and the Faujas andesitic outcrops. The Faujas root might correspond to the western part of the D1 region in the gravity model (Fig. 9B and C), and no dense anomaly is observed in this model in regard of the Dolomieu outcrop. The dense eastern border RS5 visible on the Ravine Sud radiography corresponds to the I2 region of intermediate density in the gravity model (Fig. 9).

5.3.2 *Roche Fendue radiography (Bottom of Fig. 7)*

The low-density region RF2 in the radiography corresponds to the upper part of the low-density domain L2 in the gravity model at levels 1300 and 1350 m (Figs 9A and B). This coincides with the Cratère sud region, located in the southeastern quarter of the dome (Fig. 1). The large low density domain RF4 in the radiography corresponds to rays passing through the I1 and L3 anomalies in the gravity model at levels 1250 and 1300 m (Figs 9B and C). The low density of RF4 is then in qualitative agreement with the lower densities obtained in the northeastern part of the gravity model, but the densities of I1 and L3 are not sufficiently low to quantitatively agree with the average density of RF4. This discrepancy may be due to a local deficiency of the gravity model resulting from the ill-posedness of the inversion. The RF5 dense zone in the radiography corresponds to the dense domain I1 in the gravity model. The RF1 dense border of the Roche Fendue radiography has no clear equivalent in the gravity model and could correspond to an unresolved northern extension of the dense domain I2.

6 CONCLUDING REMARKS

The standalone telescope used in this study allows long-term monitoring of the whole volcano from a single well-chosen location (Fig. 4), and the scintillator detectors forming the matrices of the telescope proved both efficient and robust with respect to the harsh environmental conditions encountered on the volcano (Marteau *et al.* 2011). Based on our experience, we expect that other types of detectors like resistive plate chambers would be difficult to control given temperature and humidity variations between night and day (e.g. Ahn *et al.* 2000; Zhang *et al.* 2010). The removal of any background noise is an issue of a great importance when performing absolute density radiography as in this study. Indeed, a background noise of a single particle per day and per scanned direction is sufficient to significantly bias the reference density. This is probably what happens at the Ravine Sud location as discussed in Section 4.2, and the telescope is being upgraded with high-frequency electronics that will enable us to measure the time-of-flight of the particles crossing the detector matrices.

The field experiments performed on Soufrière of Guadeloupe confirm that the sizing of the telescope is a good compromise between transportability (Fig. 3) and detection capabilities. The acceptance (Fig. 5) allows to obtain useful radiographies within an acquisition duration T of about 5 weeks, and the results discussed in this paper demonstrate the great interest of such quickly obtained density radiographies to reveal the inner structure of the Soufrière lava dome in relation with hazard assessment (Komorowski *et al.* 2005; Le Friant *et al.* 2006). Higher accuracy can be obtained with longer acquisition time T according to the feasibility formula established by Lesparre *et al.* (2010), and more radiographies with different angles of view must be obtained to undertake a full and stable 3-D density tomography reconstruction.

Although there is not a one-to-one correspondence between density and electrical resistivity (Section 5.2 for discussion), we found a remarkably good correlation between the density radiographies (Fig. 7) and the corresponding apparent resistivity pseudo-sections (Fig. 8). The agreement between the density radiographies and a density model obtained by inverting gravity data is also satisfactory despite the non-uniqueness of the gravity inversion. Such an accordance between muon density, electrical resistivity and gravity-inverted density constitutes a strong encouragement to develop joint inversions of these data. We may expect that the addition of muon data could efficiently regularize the non-linear inversion of electrical resistivity data, and this will be the subject of forthcoming papers.

ACKNOWLEDGMENTS

Field operations received the invaluable help from colleagues of the Guadeloupe Volcano Observatory and from the crews of the helicopter station of the French Civil Security (www.helico-dragon.com). The installation of the telescope received advices and authorization from the Director of the National Natural Park of Guadeloupe (www.guadeloupe-parcnational.fr). On the field, the maintenance and the servicing of the telescope are ensured by Fabrice Dufour. The construction of the telescopes benefited from the expertise of Bruno Carlus (computer), Bruno Kergosien (electronics), Pascal Rolland (mechanical engineering), and Sylvain Vanzetto (optical fibres). Very constructive reviews were provided by H. Tanaka and an anonymous Referee. The DIAPHANE project is financially supported by the IPGP (www.ipgp.fr) BQR grant, the DOMOSCAN ANR (www.agence-nationale-recherche.fr) project, the CNRS/IN2P3 (www.cnrs.fr) Astroparticles program. The recent eruptive history of the volcano has been improved in the framework of the CASAVA ANR project. This is IPGP contribution 3292.

REFERENCES

Abu-Zayyad, T. *et al.*, 2001. Measurement of the cosmic-ray energy spectrum and composition from 1017 to 1018.3 eV using a hybrid technique, *Astrophys. J.,* **557,** 686–699.

Ahn, S.H. *et al.*, 2000. Temperature and humidity dependence of bulk resistivity of bakelite for resistive plate chambers in CMS, *Nucl. Instr. Methods A,* **451,** 582–587.

Barrett, P.H., Bollinger, L.M., Cocconi, G., Eisenberg, Y. & Greisen, K., 1952. Interpretation of cosmic-ray measurements far underground, *Rev. Modern Phys.,* **24,** 133–178.

Bernard, M.-L., 1999. Étude expérimentale des propriétés physiques des roches pyroclastiques de la Montagne Pelée, *PhD thesis*, Université Paris 7—Denis Diderot, 326 pp.

Biot, M., 1837. Note sur la dernière éruption boueuse du volcan de la Guadeloupe, *C. R. Acad. Sci. Paris,* 651–654.

Boichu, M., Villemant, B. & Boudon, G., 2008. A model for episodic degassing of an andesitic magma intrusion, *J. geophys. Res.,* **113,** B07202, doi:10.1029/2007JB005130.

Boichu, M., Villemant, B. & Boudon, G., 2011. Degassing at La Soufrière de Guadeloupe Volcano (Lesser Antilles) since the Last Eruptive Crisis in 1975–77: result of a Shallow Magma Intrusion?, *J. Volc. Geotherm. Res.,* **203,** 102–112.

Boudon, G., Le Friant, A., Komorowski, J.-C., Deplus, C. & Semet, M.P., 2007. Volcano flank instability in the Lesser Antilles Arc: diversity of scale, processes, and temporal recurrence, *J. geophys. Res.,* **112,** doi:10.1029/2006JB004674.

Boudon, G., Komorowski, J.-C., Villemant, B. & Semet, M.P., 2008. A new scenario for the last magmatic eruption of La Soufrière of Guadeloupe (Lesser Antilles) in 1530 A.D. Evidence from stratigraphy radiocarbon dating and magmatic evolution of erupted products, *J. Volc. Geotherm. Res.,* **178,** 474–490, doi:10.1016/j.jvolgeores.2008.03.006.

Caffau, E., Coren, F. & Giannini, G., 1997. Underground cosmic-ray measurement for morphological reconstruction of the Grotta Gigante natural cave, *Nucl. Instrum. Methods A,* **385,** 480–488.

Calcagno, Ph., Chils, J.-P., Courrioux, G. & Guillen, A., 2008. Geological modelling from field data and geological knowledge: part I. Modelling method coupling 3D potential-field interpolation and geological rules, *Phys. Earth planet. Inter.,* **171,** 147–157.

Coutant, O., Bernard, M.L., Beauducel, F., Nicollin, F., Bouin, M.P. & Roussel, S., 2012. Joint inversion of P-wave velocity and density, application to La Soufrière of Guadeloupe upper geothermal system, Lesser Antilles, *Geophys. J. Int.,* submitted.

Feuillard, M., Allegre, C.J., Brandeis, G., Gaulon, R., Le Mouël, J.L., Mercier, J.C., Pozzi, J.P. & Semet, M.P., 1983. The 19751977 crisis of La Soufrière de Guadeloupe (F.W.I.): a still-born magmatic eruption, *J. Volc. Geotherm. Res.,* **16,** 317–334, doi:10.1016/0377-0273(83)90036-7.

Gaisser, T. & Stanev, T., 2008. Cosmic rays, *Phys. Lett. B,* **667,** 254–260, doi:10.1016/j.physletb.2008.07.028.

Gibert, D., Beauducel, F., Déclais, Y., Lesparre, N., Marteau, J., Nicollin, F. & Tarantola, A., 2010. Muon tomography: plans for observations in the Lesser Antilles, *Earth Planets Space,* **62,** 153–165.

Golden, R.L. *et al.*, 1995. Measurement of the energy spectra of cosmic ray electron component and protons at ground level, *J. geophys. Res.,* **100,** 23 515–23 522.

Guillen, A., Calcagno, Ph., Courrioux, G., Joly, A. & Ledru, P., 2008. Geological modelling from field data and geological knowledge: part II. Modelling validation using gravity and magnetic data inversion, *Phys. Earth planet. Inter.,* **171,** 158–169.

Gunawan, H., 2005. Gravimétrie et microgravimétrie appliquées à la volcanologie: exemples de la Soufrière de Guadeloupe et du Mérapi, *PhD thesis*, Institut de Physique du Globe de Paris, 198 pp.

Hebbeker, T. & Timmermans, C., 2002. A compilation of high energy atmospheric muon data at sea level, *Astropart. Phys.,* **18,** 107–127.

Kirsch, R. & Yaramanci, U., 2009. Geoelectrical methods, in *Groundwater Geophysics,* pp. 85–117, ed. Kirsch, R., Springer, Berlin.

Komorowski, J.-C., 2008. Du volcan au pyroclaste: une approche pluridisciplinaire de la compréhension des processus éruptifs et de l'évaluation des aléas. Mémoire dHabilitation à Diriger des Recherches, Université René Diderot Paris 7, spécialité: Sciences de la Terre, de l'environnement et des planètes, 549pp.

Komorowski, J.-C. *et al.*, 2001. L'activité éruptive et non-éruptive de la Soufrière de Guadeloupe: problèmes et implications de la phénoménologie et des signaux actuellement enregistrés, Atelier Les volcans antillais: des processus aux signaux PNRN CNRS INSU, 2001 January 18–19, Paris, pp. 18–21.

Komorowski, J.-C., Boudon, G., Semet, M., Villemant, B. & Hammouya, G., 2002. Recurrent flank-collapses at Soufrière of Guadeloupe Volcano: implications of acid hydrothermal fluids on edifice stability Mount Pelée 1902–2002; explosive volcanism in subduction zones, IPGP–INSU–IAVCEI International Congress, Ile de la Martinique, 12–16 mai 2002, p. 69. abstract volume.

Komorowski, J.C., Boudon, G., Semet, M., Beauducel, F., Anténor-Habazac, C., Bazin, S. & Hammouya, G., 2005. Guadeloupe, in *Volcanic Atlas of the Lesser Antilles,* pp. 65–102, eds Lindsay, J.M., Robertson, R.E.A., Shepherd, J.B. & Ali, S., Seismic Research Unit, The University of the West Indies, Trinidad and Tobago.

Komorowski, J.C., Legendre, Y., Caron, B. & Boudon, G., 2008. Reconstruction and analysis of sub-plinian tephra dispersal during the 1530 A.D. Soufrière (Guadeloupe) eruption: implications for scenario definition and hazards assessment, *J. Volc. Geotherm. Res.,* **178,** 491–515, doi:10.1016/j.jvolgeores.2007.11.022.

Kudryavtsev, V.A., 2009. Muon simulation codes MUSIC and MUSUN for underground physics, *Comp. Phys. Comm.,* **180,** 339–346.

Kuster, D. & Silve, V., 1997. *Guadeloupe, Canyons, Gouffres, Découverte,* Editions Gap, La Ravoire, Chambéry, 256pp.

Lecomte, J., 1963. Évaluation des coïncidence fortuites dans un montage à coïncidence du type 'lent-rapide', *Nucl. Instrum. Methods,* **24,** 165–171.

Le Friant, A., Boudon, G., Komorowski, J.C., Heinrich, P. & Semet, M.P., 2006. Potential flank-collapse of Soufrière Volcano, Guadeloupe, lesser Antilles? Numerical simulation and hazards, *Nat. Hazards,* **39,** 381–393, doi:10.1007/s11069-005-6128-8.

Le Guern, F., Bernard, A. & Chevrier, R.M., 1980. Soufrière of Guadeloupe 1976–1977: eruption-mass and energy transfer and volcanic health hazards, *Bull. Volcanol.,* **43,** 577–593.

Leparoux, D., Gibert, D. & Côte, Ph., 2001. Adaptation of prestack migration to multi-offset ground-penetrating radar (GPR) data, *Geophys. Prospect.,* **49,** 374–386.

Lesparre, N., Gibert, D., Marteau, J., Déclais, Y., Carbone, D. & Galichet, E., 2010. Geophysical muon imaging: feasibility and limits, *Geophys. J. Int.,* **183,** 1348–1361.

Lesparre, N., Gibert, D. & Marteau, J., 2012. Bayesian dual inversion of experimental telescope acceptance and integrated flux for geophysical muon tomography, *Geophys. J. Int.,* **188,** 490–497, doi: 10.1111/j.1365-246X.2011.05268.x.

L'Herminier, F., 1815. Suite aux réflexions géologiques sur les volcans et considérations sur la Guadeloupe, *J. Phys. Chimie Hist. Nat. Arts,* **81,** 207–217.

Li, Y. & Oldenburg, D., 1998. 3-D inversion of gravity data, *Geophysics,* **63,** 109–119.

Maineult, A., Bernab´, Y. & Ackerer, P., 2006. Detection of advected, reacting redox fronts from self-potential measurements, *J. Contam. Hydrol.,* **86,** 32–52.

Marteau, J., Gibert, D., Lesparre, N., Nicollin, F., Noli, P. & Giacoppo, F., 2011. Muons tomography applied to geosciences and volcanology, *Nucl. Instr. Methods A,* in press, doi:10.1016/j.nima.2011.11.061.

Mouret, C. & Rodet, J., 1985. La salle Jules Verne, grand volume souterrain d'un édifice volcanique andésitique, Soufrière de Guadeloupe, *Mém. Spéléo Club Paris,* **12,** 43–54.

Nagamine, K., 2003. *Introductory Muon Science,* Cambridge University Press, Cambridge, 208pp.

Nagamine, K., 1995. Geo-tomographic observation of inner-structure of volcano with cosmic-ray muons, *J. Geography,* **104,** 998–1007.

Nagamine, K., Iwasaki, M., Shimomura, K. & Ishida, K., 1995. Method of probing inner-structure of geophysical substance with the horizontal cosmic-ray muons and possible application to volcanic eruption prediction, *Nucl. Instr. Meth. A,* **356,** 585–595.

Nicollin, F., Gibert, D., Beauducel, F., Boudon, G. & Komorowski, J.-C., 2006. Electrical tomography of La Soufrière of Guadeloupe Volcano: field experiments, 1D inversion and qualitative interpretation, *Earth planet. Sci. Lett.,* **244,** 709–724.

Observatoire Volcanologique et Sismologique de la Guadeloupe (OVSG–IPGP), 1999–2011. *Bilan Mensuel de l'Activité Volcanique de la Soufrière et de la Sismicité Régionale*, Observatoire Volcanologique et Sismologique de la Guadeloupe, Institut de Physique du Globe de Paris, IPGP–CNRS–INSU Conseil Général de Guadeloupe, http://www.ipgp.jussieu.fr/pages/0303040901.php.

Parasnis, D.S., 1997. *Principles of Applied Geophysics,* Springer, Berlin, 429pp.

Pessel, M. & Gibert, D., 2003. Multiscale electrical impedance tomography, *J. geophys. Res.,* **108,** doi:10.1029/2001JB000233.

Salaün, A., Villemant, B., Gérard, M., Komorowski, J.-C. & Michel, A., 2011. Hydrothermal alteration in andesitic volcanoes: trace element redistribution in active and ancient hydrothermal systems of Guadeloupe (Lesser Antilles), *J. Geochem. Explor.,* **111,** 59–83, doi:10.1016/j.gexplo.2011.06.004.

Tanaka, H., Nagamine, K., Nakamura, S.N. & Ishida, K., 2005. Radiographic measurements of the internal structure of Mt. West Iwate with near horizontal cosmic ray muons and future developments, *Nucl. Instrum. Methods A,* **555,** 164–172.

Tanaka, H., Nakano, T., Takahashi, S., Yoshida, J., Ohshima, H., Maekawa, T., Watanabe, H. & Niwa, K., 2007a. Imaging the conduit size of the dome with cosmic ray muons: the structure beneath Showa Shinzan Lava Dome, Japan, *Geophys. Res. Lett.,* **34,** L22311, doi:10.1029/2007GL031389.

Tanaka, H. *et al.*, 2007b. High resolution imaging in the inhomogeneous crust with cosmic-ray muon radiography: the density structure below the volcanic crater floor of Mt. Asama, Japan, *Earth planet. Sci. Lett.,* **263,** 104–113.

Tanaka, H. *et al.*, 2008. Radiographic imaging below a volcanic crater floor with cosmic-ray muons, *Am. J. Sci.,* **308,** 843–850.

Tanaka, H., Uchida, T., Tanaka, M., Shinohara, H. & Taira, H., 2009a. Cosmic-ray muon imaging of magma in a conduit: degassing process of Satsuma Iwojima Volcano, Japan, *Geophys. Res. Lett.,* **36,** L01304, doi:10.1029/2008GL036451.

Tanaka, H. *et al.*, 2009b. Detecting a mass change inside a volcano by cosmic-ray muon radiography (muography): first results from measurements at Asama volcano, Japan, *Geophys. Res. Lett.,* **36,** L17302, doi:10.1029/2009GL039448.

Tang, A., Horton-Smith, G., Kudryavtsev, V.A. & Tonazzo, A., 2006. Muon simulations for Super-Kamiokande, KamLAND, and CHOOZ, *Phys. Rev. D,* **74,** 053007, doi:10.1103/PhysRevD.74.053007.

Villemant, B., Hammouya, G., Michel, A., Semet, M., Komorowski, J.C., Boudon, G. & Cheminée, J.L, 2005. The memory of volcanic waters: shallow magma degassing revealed by halogen monitoring in thermal springs of La Soufrière volcano (Guadeloupe, Lesser Antilles), *Earth planet. Sci. Lett.,* **237,** 710–728, doi:10.1016/j.epsl.2005.05.013.

Zhang, Q., Bilki, B., Butler, J., May, E., Mavromanolakis, G., Norbeck, E., Repond, J., Underwood, D. & Xia, L., 2010. Environmental dependence of the performance of resistive plate chambers, *J. Instrum.,* **5,** P02007, doi:10.1088/1748-0221/5/02/P02007.

Zhdanov, M., 2009. *Geophysical Electromagnetic Theory and Methods,* Elsevier, Amsterdam, 848pp.